

# DEGRADATION-AWARE ALL-IN-ONE IMAGE RESTORATION VIA LATENT PRIOR ENCODING

**S. M. A. Sharif Abdur Rehman Fayaz Ali Dharejo Radu Timofte\* Rizwan Ali Naqvi\***  
 Code available: [github.com/sharif-apu/DAIR](https://github.com/sharif-apu/DAIR)

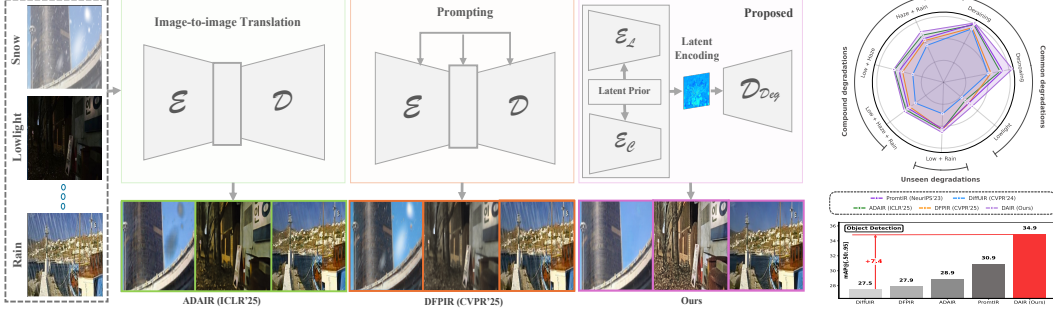


Figure 1: Comparison of common all-in-one image restoration paradigms. Existing approaches depend on explicit task-specific guidance through manual prompts or predefined architectural biases. Our DAIR learns degradation-aware representations directly from degraded images through latent prior inference.

## ABSTRACT

Real-world images often suffer from spatially diverse degradations such as haze, rain, snow, and low-light, significantly impacting visual quality and downstream vision tasks. Existing all-in-one restoration (AIR) approaches either depend on external text prompts or embed hand-crafted architectural priors (e.g., frequency heuristics); both impose discrete, brittle assumptions that weaken generalization to unseen or mixed degradations. To address this limitation, we propose to reframe AIR as learned latent prior inference, where degradation-aware representations are automatically inferred from the input without explicit task cues. Based on latent priors, we formulate AIR as a structured reasoning paradigm: (1) which features to route (adaptive feature selection), (2) where to restore (spatial localization), and (3) what to restore (degradation semantics). We design a lightweight decoding module that efficiently leverages these latent encoded cues for spatially-adaptive restoration. Extensive experiments across six common degradation tasks, five compound settings, and previously unseen degradations demonstrate that our method outperforms state-of-the-art (SOTA) approaches, achieving an average PSNR improvement of 1.68 dB while being three times more efficient.

## 1 INTRODUCTION

Real-world images are frequently degraded by factors like haze, rain, snow, low-light, and motion blur Tian et al. (2025a); Jiang et al. (2025). These spatially varying degradations may occur alternately or even overlap, depending on environmental and capture conditions Guo et al. (2024). Such entangled degradation patterns significantly reduce visual quality, resulting in impaired downstream vision tasks Tian et al. (2025a); Jiang et al. (2025). Recent deep learning-based single-task methods Dong et al. (2020); Valanarasu et al. (2022); Chen et al. (2021); Cai et al. (2023); Wang et al. (2022); Zhang et al. (2017) have made significant progress in addressing individual restoration challenges. However, deploying separate task-specific (TS) networks for each degradation type is computationally expensive and impractical, driving interest in AIR frameworks Jiang et al. (2025).

\*Radu Timofte and Rizwan Ali Naqvi are the corresponding authors.

---

Current AIR approaches can be broadly categorized into two paradigms. (1) Adaptive feature learning methods, such as ADAIR Cui et al. (2024) and AirNet Li et al. (2022), utilize hand-crafted frequency priors or architectural inductive biases to automatically differentiate degradation types. Although these methods circumvent manual specification, they inherently depend on pre-defined assumptions about degradation characteristics, which often fail to generalize to novel or compound corruptions Gao et al. (2024). (2) Prompt-based restoration methods, such as PromptIR Vaishnav et al. (2023) and DFPIR Tian et al. (2025a), rely on explicit, manually provided prompts to guide the restoration network by specifying degradation types. These methods offer flexible control but face a fundamental "chicken-and-egg" dilemma: in real-world scenarios, the degradation type and location are rarely known beforehand, yet the network requires this information to perform effective restoration Jiang et al. (2025). Moreover, TS instructions constrain generalization, particularly in cases of mixed degradations or varying homogeneous degradations (e.g., different noise levels). As illustrated in Fig. 1, both existing AIR paradigms have limited robustness and practical applicability in unconstrained environments.

To overcome these limitations, we reframe AIR as a latent prior inference problem. Unlike existing methods Vaishnav et al. (2023); Cui et al. (2024); Tian et al. (2025a) that rely on explicit degradation prompting or predefined architectural inductive biases, we propose learning degradation-aware representations directly from the degraded image through a multi-level feature descriptor inspired by the variational autoencoder (VAE) Kingma & Welling (2013). Our learned prior eliminates the need for manual degradation hints and enables spatially adaptive restoration of diverse and unseen degradations. Guided by these learned priors, the proposed degradation-aware AIR (DAIR) framework incorporates a "where, which, what" reasoning paradigm: it learns degradation-aware feature selection (which), localizes corrupted regions using spatial attention maps (where), and adaptively fuses multi-scale global representations (what). Our unified strategy substantially enhances the flexibility and generalizability of blind restoration methods.

### Our contributions are:

- We propose reframe AIR to directly learn latent degradation priors from the corrupted image, eliminating the need for external manual prompts (MP).
- We propose a reasoning image restoration paradigm comprising: (1) latent priors for learning degradation-aware representations, enabling decisions on "which" encoder features to utilize for reconstruction; (2) spatially-adaptive degradation map (DM) that integrate frequency-domain cues with efficient element-wise attention, providing interpretable and localized restoration guidance on "where" to focus beyond implicit attention; (3) cross-modal fusion of structural and color cues with global degradation priors via adaptive scaling and shifting to determine "what" content to reconstruct; and (4) a decoder with linear complexity performing explicit spatial reasoning for leverages 1-3 cues, we termed it 3WD (which–where–what decoding).
- DAIR consistently outperforms SOTA on six common restoration tasks (e.g., snow, low-light), five compound degradations (e.g., haze + rain, low-light + haze + rain), and unseen degradations, achieving an average 1.68 dB PSNR gain. It also improves downstream tasks on images with unknown multi-type degradations, e.g., boosting YOLOv12-L Tian et al. (2025b) object detection by up to 7.40 mAP over SOTA AIR methods, highlighting strong generalizability (Fig. 1).

## 2 RELATED WORKS

### 2.1 IMAGE-TO-IMAGE TRANSLATION

Early image restoration methods were designed to address individual TS settings, such as denoising Zhang et al. (2017); Pang et al. (2021); Zhang et al. (2018a), dehazing Dong et al. (2020); Qin et al. (2020), deraining Jiang et al. (2020); Ren et al. (2019), low-light image enhancement (LLIE) Wei et al. (2018); Yi et al. (2023), or deblurring Cho et al. (2021); Nah et al. (2017). These task-dependent approaches achieved impressive results; their limited scope prevented generalization across diverse restoration challenges. Transformer-based models, such as Restormer Zamir et al. (2022) and Uformer Wang et al. (2022), have explored multiple degradation scenarios; however, they still require separate training for individual tasks. To address this, recent methods shift towards AIR, aiming to handle diverse degradations within a unified framework. AirNet Li et al. (2022) pi-

oneered this field by introducing contrastive learning to extract degradation representations, guiding restoration for unknown corruptions. ADAIR Cui et al. (2024) recalibrate features using adaptive frequency statistics, enabling task-agnostic restoration. Recent methods, such as DiffUIR Zheng et al. (2024), have also explored generative techniques (i.e., latent diffusion Rombach et al. (2022)). These unified approaches mark a significant step forward, minimizing TS training and advancing toward generalizable AIR solutions.

## 2.2 PROMPT-GUIDED ALL-IN-ONE RESTORATION

Image-to-image translation-based method commonly fails in separating unique degradations Brooks et al. (2023); Jiang et al. (2025). To counter this, recent AIR Gao et al. (2024); Vaishnav et al. (2023); Tian et al. (2025a) methods have incorporated MP to provide prior knowledge of degradation cues. PromptIR Vaishnav et al. (2023) integrates text-based prompts into a transformer framework, leveraging degradation-specific semantic information to guide the restoration process. OneRestore Guo et al. (2024) introduced visual and text prompts within a transformer-based framework to encode TS information. Recently, DFPIR Tian et al. (2025a) introduced a degradation-aware feature perturbation method that utilizes CLIP-encoded Radford et al. (2021) text prompts to guide channel shuffling and attention masking, enabling unified restoration across diverse degradations. UHD-Processor Liu et al. (2025) introduced a VAE-based framework with progressive frequency learning and MP for ultra-high-definition image restoration. Notably, unlike UHD-Processor and other prompt-based methods, our method learns latent degradation representations directly from the input, enabling blind restoration without user guidance.

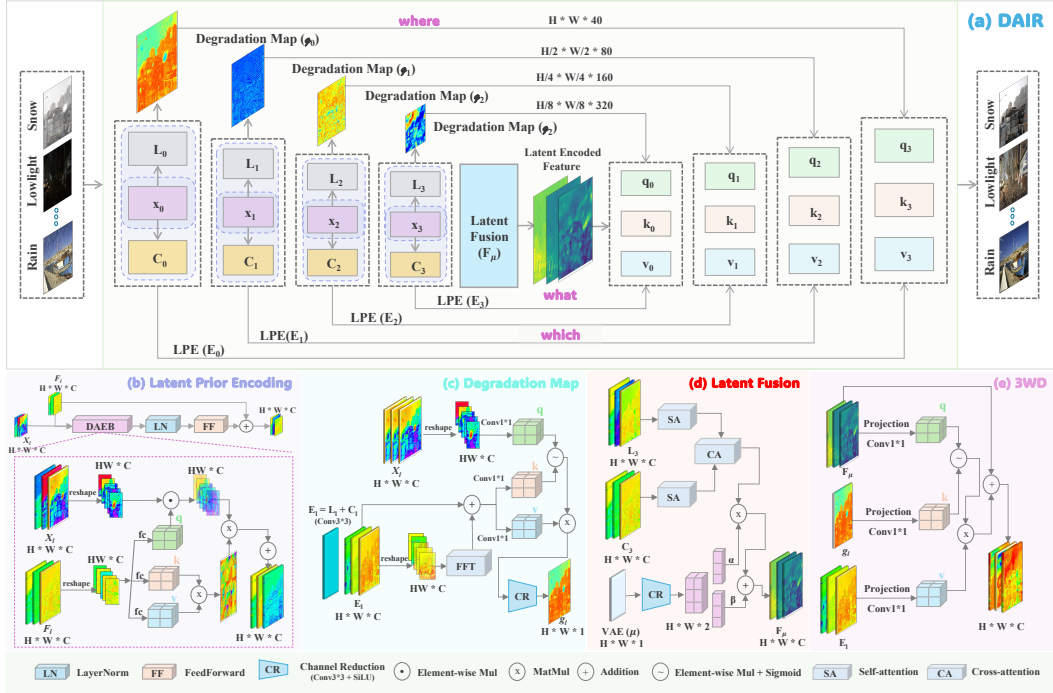


Figure 2: Overview of the proposed DAIR framework: (a) Overall architecture, (b) Latent prior encoding (*which*), (c) Degradation mapping (*where*), (d) Latent fusion (*what*), (e) 3WD restoration module. Best viewed with Zoom.

## 3 METHOD

**Overall pipeline.** Fig. 2 illustrates the details of our framework. Given a degraded input image  $\mathbf{I}_{deg} \in \mathbb{R}^{3 \times H \times W}$  with unknown degradation  $\mathcal{D}_R$ , our framework learn to infer stage-wise latent codes  $xl$  ( $l = 0, \dots, 3$ ) and a bottleneck global descriptor  $\mu$ , serving as degradation priors. The encoder employs a two-branch architecture that separately processes multi-scale structural features

---

(e.g., luminance  $L_\ell$ ) and color features (e.g., chrominance  $C_\ell$ ), enabling more effective representation of both spatial and chromatic information Sharif et al. (2025); Yan et al. (2025). At each stage,  $L_\ell$  and  $C_\ell$  interact with  $x_\ell$  via *Degradation-Aware Encoder Blocks* (DAEB), leveraging degradation information into the feature extraction process. The branches are fused as  $F_\ell = L_\ell + C_\ell$  and used as residual refined feature propagation to the decoder. Concurrently, a mapping block transforms  $(L_\ell, C_\ell, x_\ell)$  into a compact DM  $g_\ell$ , which is also forwarded to the decoder for explicit degradation localization guidance. At the bottleneck, a  $\mu$ -guided fusion block merges the deepest LC features with the global degradation latent using adaptive scaling and shifting Perez et al. (2018), resulting in  $F_\mu = \gamma \odot [L_3 + C_3] + \beta$ . The decoder reconstructs the clean image from  $F_\mu$ , leveraging the degradation focus map  $g_\ell$  and the selected features  $F_\ell$  derived from latent priors. This architecture enables the model to automatically identify and restore a wide range of degradations without explicit user input or task specification.

### 3.1 LEARNING DEGRADATION REASONING WITH LATENT PRIOR

We propose a multi-scale latent descriptor Kingma & Welling (2013) that directly infers continuous degradation representations from corrupted images without user-guided MP. Given  $\mathbf{I}_{deg} \in \mathbb{R}^{3 \times H \times W}$ , the encoder extracts hierarchical feature maps  $\{\mathbf{x}_\ell\}_{\ell=0}^3$  using convolutional layers and residual channel-attention Hu et al. (2018) blocks that emphasize degradation-relevant cues. At the deepest stage, multi-head self-attention Vaswani et al. (2017) refines the features to obtain the bottleneck representation  $\mathbf{z}$ . The VAE parameterizes a distribution with  $\mu = f_\mu(\mathbf{z})$  and  $\log \sigma^2 = f_\sigma(\mathbf{z})$ , sampling  $\mathbf{z}_{reparam} = \mu + \sigma \odot \epsilon$  where  $\epsilon \sim \mathcal{N}(0, \mathbf{I})$ . The decoder reconstructs the input image from the sampled latent. This multi-objective training ensures that hierarchical features  $\{\mathbf{x}_\ell\}$  capture degradation-specific representations at multiple scales, while bottleneck statistics  $\mu$  encode global degradation semantics. Both serve as degradation-aware latent cues to condition the restoration model:

$$\text{VAE}(\mathbf{I}_{deg}) = \{\mathbf{x}_\ell\}_{\ell=0}^3, \mu. \quad (1)$$

#### 3.1.1 LATENT PRIOR ENCODING

Unlike existing methods (PromptIR Vaishnav et al. (2023), DFPIR Tian et al. (2025a), CAPTNet Gao et al. (2024)) that inject prompts during decoding, we inject VAE-derived degradation priors during encoding. This enables our encoders to generate both degradation-aware and degradation-agnostic skip connections, providing richer guidance for reconstruction. We separately encode the luminance and chrominance (LC) components Smith (1978) ( $\mathbf{L}_{deg}, \mathbf{C}_{deg}$ ) of the degraded input using dedicated LC encoders Yan et al. (2025); Sharif et al. (2025) for better structural and chromatic information. Fig. 2 (b) illustrates our latent prior encoding. Two parallel encoders,  $\mathcal{E}_L(\cdot)$  and  $\mathcal{E}_C(\cdot)$ , process these components across multiple scales using DAEB. At stage  $\ell$ , we injects latent degradation priors  $\mathbf{x}_\ell$  via value modulation:

$$Q_\ell = \mathbf{f}_\ell W_Q, \quad K_\ell = \mathbf{f}_\ell W_K, \quad \tilde{V}_\ell = (\mathbf{f}_\ell W_V) \odot \mathbf{x}_\ell \quad (2)$$

where  $\mathbf{f}_\ell \in \{\mathbf{f}_\ell^L, \mathbf{f}_\ell^C\}$  are intermediate features. The attention mechanism produces degradation-aware representations as DAEB( $\mathbf{f}_\ell, \mathbf{x}_\ell$ ) =  $\text{softmax}(Q_\ell K_\ell^\top / \sqrt{d}) \tilde{V}_\ell$ . Combining these components, the encoder outputs at each stage are:

$$L_\ell = \mathcal{E}_\ell^L(\mathbf{L}_{deg}, \mathbf{x}_\ell), \quad C_\ell = \mathcal{E}_\ell^C(\mathbf{C}_{deg}, \mathbf{x}_\ell) \quad (3)$$

At each stage, latent-derived priors  $\mathbf{x}_\ell$  modulate the value features after multi-head projection, enabling semantically refined propagation that preserves both degradation-specific and clean structural information. During decoding, these priors serve as selective feature utilization for effective reconstruction.

#### 3.1.2 LEARNABLE DEGRADATION MAP

Traditional skip connections propagate noise from degraded inputs to the decoder, without spatial awareness of the degradation Mao et al. (2016). We counter these limitations with learnable DM that encode spatially-varying degradation patterns for effective reconstruction (Fig. 2 (c)). At encoder stage  $\ell$ , our *Degradation Mapping Block* generates scale-specific maps  $g_\ell$  from LC features  $L_\ell, C_\ell$  and latent prior encoding  $\mathbf{x}_\ell$ . We first fuse complementary LC information:  $\mathbf{f}_\ell^{LC} = \text{Conv}_{3 \times 3}(L_\ell +$

$C_\ell$ ). To capture frequency-domain degradation characteristics, we enhance features with spectral information via Fast Fourier Transform Cooley & Tukey (1965):  $\mathcal{F}(L_\ell) = \text{FFT}(L_\ell - \mu(L_\ell))$ ,  $\mathcal{F}(C_\ell) = \text{FFT}(C_\ell - \mu(C_\ell))$ . The magnitude and phase components are concatenated and projected:

$$\mathbf{f}_\ell^{\text{freq}} = \text{ReLU}(\text{Conv}_{1 \times 1}([\|\mathcal{F}(L_\ell)\| \|\mathcal{F}(C_\ell)\| \|\angle\mathcal{F}(L_\ell)\| \|\angle\mathcal{F}(C_\ell)\|])), \quad \tilde{\mathbf{f}}_\ell^{LC} = \mathbf{f}_\ell^{LC} + \mathbf{f}_\ell^{\text{freq}} \quad (4)$$

For computational efficiency, we employ element-wise attention:

$$Q_\ell = \text{Conv}_{1 \times 1}(\tilde{\mathbf{f}}_\ell^{LC}), \quad K_\ell = V_\ell = \text{Conv}_{1 \times 1}(\mathbf{x}_\ell) \quad (5)$$

$$\mathbf{A}_\ell = \sigma(Q_\ell \odot K_\ell), \quad \mathbf{y}_\ell = \mathbf{A}_\ell \odot V_\ell \quad (6)$$

where  $\sigma$  is sigmoid activation and  $\odot$  denotes Hadamard product. The DM is generated via residual refinement:

$$g_\ell = \phi_{\text{map}}(\text{ReLU}(\text{Conv}_{3 \times 3}(\mathbf{y}_\ell + \tilde{\mathbf{f}}_\ell^{LC}))) \quad (7)$$

where  $\phi_{\text{map}}$  is a two-layer convolutional head producing  $g_\ell \in \mathbb{R}^{1 \times H_\ell \times W_\ell}$ . This design captures spatial-frequency degradation patterns with linear complexity, while providing interpretable and localized restoration guidance.

### 3.1.3 LATENT ENCODED FUSION

At the encoder bottleneck, we leverage the deepest LC features  $\mathbf{L}_3, \mathbf{C}_3 \in \mathbb{R}^{B \times 320 \times \frac{H}{8} \times \frac{W}{8}}$ , along with the latent global descriptor  $\mu$ . As shown in Fig. 2 (d), our fusion mechanism integrates three components: (i) intra-branch self-attention Sharif et al. (2025); Cai et al. (2023) for independent modality refinement, where  $\hat{\mathbf{L}}_3 = \text{MHSA}(\mathbf{L}_3)$  and  $\hat{\mathbf{C}}_3 = \text{MHSA}(\mathbf{C}_3)$ ; (ii) cross-branch attention Sharif et al. (2025) for complementary information exchange, where chrominance attends to luminance:  $\mathbf{F} = \text{LayerNorm}(\text{MHCA}(\hat{\mathbf{C}}_3, \hat{\mathbf{L}}_3) + \hat{\mathbf{C}}_3 + \hat{\mathbf{L}}_3)$ , enabling the model to leverage structural and color information while preserving individual branch characteristics; and (iii) adaptive feature modulation conditioned on the global degradation prior  $\mu$ , combining LC features through adaptive scaling and shifting for TS feature modulation while maintaining underlying image characteristics. Unlike standard FiLM Perez et al. (2018) that applies uniform modulation, our approach makes degradation-aware reconstruction:

$$[\gamma_{\text{struct}}, \beta_{\text{color}}] = \phi_\mu(\mu), \quad \gamma_{\text{struct}}, \beta_{\text{color}} \in \mathbb{R}^{B \times 320 \times \frac{H}{8} \times \frac{W}{8}} \quad (8)$$

$$\mathbf{F}_\mu = \mathbf{F}_{\text{LC}} \odot (1 + \gamma_{\text{struct}}) + \beta_{\text{color}} \quad (9)$$

where  $\phi_\mu$  serves as a content decision network (two  $1 \times 1$  convolutions with SiLU) that determines what structural and chromatic content should be reconstructed based on inferred degradation characteristics. Our **identity-anchored scaling**  $(1 + \gamma_{\text{struct}})$  ensures content reconstruction decisions are made as learned adjustments around the original cross-modal features, completing our “what” reasoning component.

## 3.2 DEGRADATION-AWARE RECONSTRUCTION

The proposed decoder addresses our fundamental reasoning questions by reconstructing images through the 3WD module (Fig. 2 (e)). At each decoder stage  $\ell$ , given upsampled features  $U_{\ell-1}$  and combined encoder features  $E_\ell = L_\ell + C_\ell$ , we compute linear attention projections:

$$Q_\ell = W_Q^{(\ell)} U_{\ell-1}, \quad K_\ell = W_K^{(\ell)} g_\ell, \quad V_\ell = W_V^{(\ell)} E_\ell$$

Degradation-guided attention operates as  $A_\ell = \sigma(Q_\ell \odot K_\ell)$ , enabling  $g_\ell$  to directly modulate spatial restoration. Features are updated through:

$$D_\ell = \phi_\ell(A_\ell \odot V_\ell + U_{\ell-1}) \quad (10)$$

Notably, our proposed 3WD achieves linear computational complexity of  $O(HW)$  per stage, in contrast to the quadratic complexity  $O(H^2W^2)$  of standard attention mechanisms Vaswani et al. (2017). This efficiency stems from utilizing element-wise multiplication ( $\odot$ ) between tensors of shape  $H \times W \times C$ , requiring exactly  $HW \times C$  operations. We perceive final reconstruction with learned features and global residual:  $\hat{\mathbf{I}} = \tanh(W_{\text{rec}} D_1) + \mathbf{I}_{\text{deg}}$ .

## 4 EXPERIMENTS

### 4.1 SETUP

**Dataset and methods.** We evaluated our method under two degradation scenarios: common (non-overlapping) degradations and compound (overlapping) settings. For common degradations, we tested on standard tasks/datasets, including dehazing (SOTS Li et al. (2018)), deraining (Rain100L Fu et al. (2017)), desnowing (CCD Li et al. (2020)), deblurring Nah et al. (2017), deblurring (Go-Pro Nah et al. (2017)), denoising (DIV2K Agustsson & Timofte (2017)) with random noise levels ( $\sigma \in [0, 50]$ ) to improve generalization, and LLIE using the LSD dataset Sharif et al. (2025), captured in uncontrolled environments. In compound degradation, we employed the CDD dataset Guo et al. (2024), combining five degradations (e.g., haze+rain, low-light+haze+snow). Subsets like haze+snow and low-light+rain were reserved for testing generalization comparison on unseen degradations. Ablation and analysis, we combined four common tasks (denoising, desnowing, deraining, and LLIE) to analyze consistency.

We compared DAIR against transformer-based baseline methods (Uformer Wang et al. (2022), Restormer Zamir et al. (2022)), SOTA AIR approaches (ADAIR Cui et al. (2024), AIRNet Li et al. (2022)), prompting-based methods (DFPIR Tian et al. (2025a), PromptIR Vaishnav et al. (2023)), and diffusion-based latent enhancement (DiffUIR Zheng et al. (2024)). Single-task benchmarks included deraining (HDCWNet Zhu et al. (2021), TransWeather Valanarasu et al. (2022)), Retinex-based LLIE (RetinexNet Wei et al. (2018), Diff-Retinex Yi et al. (2023)).

**Implementation** We first pre-train our latent encoder for 200,000 steps, combining six single and five compound (known) degradations using a composite loss (self-reconstruction + KL Kingma & Welling (2014) + discriminative latent regularizer Guo et al. (2023)). The resulting encoder is frozen and reused for all single, compound, and unseen degradation experiments without any fine-tuning. We only tune the main network for TS settings using the combination of L1 and SSIM losses for fair comparison. This network has been trained for 100,000 to 500,000 steps, depending on task complexity. We trained both the latent encoder and the main restoration network using the Adam optimizer with hyperparameters  $\beta_1 = 0.9$ ,  $\beta_2 = 0.99$ , and learning rate = 1e-4. All training was conducted on a single NVIDIA RTX 3060 GPU with a batch size of 4, using randomly cropped  $256 \times 256$  patches as input. All baseline methods are trained using their official implementations and suggested hyperparameters to ensure fairness.

### 4.2 RESULTS ON COMMON DEGRADATION

#### 4.2.1 MULTI-TASK (6D) RESTORATION

Table 1: Performance comparison across different image restoration tasks. Best results in **bold red**, second best underlined, and increment over best performing method highlighted in **blue**.

Method	MP	Params (M)	GFLOPs <sup>1</sup>	Lowlight PSNR/SSIM↑	Dehazing PSNR/SSIM↑	Denoising PSNR/SSIM↑	Desnowing PSNR/SSIM↑	Deblurring PSNR/SSIM↑	Deraining PSNR/SSIM↑	Average PSNR/SSIM↑
Uformer Wang et al. (2022)	✗	20.63	43.86	12.10/0.4897	29.15/0.9727	27.55/0.8201	24.80/0.8832	23.67/0.8074	28.74/0.8823	24.34/0.8092
Restormer Zamir et al. (2022)	✗	26.13	141.75	<u>15.33</u> /0.6180	28.51/0.9738	20.41/0.5357	22.98/0.8585	<u>25.41</u> /0.8286	25.99/0.8164	23.10/0.7718
AIRNet Li et al. (2022)	✗	8.93	301.27	8.87/0.3655	25.92/0.9663	28.87/0.8789	19.08/0.7300	22.81/0.8067	24.92/0.8027	21.75/0.7583
PromptIR Vaishnav et al. (2023)	✓	35.59	158.14	14.73/0.5374	<u>30.41</u> /0.9580	23.96/0.6378	27.08/0.9169	26.04/0.8366	30.01/0.8992	<u>25.37</u> /0.7977
DiffUIR Zheng et al. (2024)	✓	36.26	4400.00	10.76/0.4101	30.05/0.9797	20.25/0.6859	20.39/0.8014	25.03/0.8474	27.46/0.8917	22.32/0.7694
ADAIR Cui et al. (2024)	✗	28.78	147.18	12.76/0.4974	30.15/0.9783	28.65/0.8715	25.86/0.8812	25.14/0.8200	29.56/0.8901	25.35/0.8231
DFPIR Tian et al. (2025a)	✓	31.07	151.07	14.84/0.5232	28.29/0.9709	27.78/0.8341	21.74/0.7935	26.10/0.8271	28.02/0.8372	24.46/0.7977
<b>DAIR (Ours)</b>	✗	<b>18.08</b>	<b>45.65</b>	<b>16.87/0.6661</b>	<b>34.08/0.9864</b>	<b>29.12/0.8971</b>	<b>31.50/0.9570</b>	<b>26.82/0.8793</b>	<b>30.51/0.9117</b>	<b>28.15/0.8829</b>
<i>Improvement</i>		<i>-10.70</i>	<i>-96.10</i>	<i>+1.54/+0.0481</i>	<i>+3.67/+0.0067</i>	<i>+2.25/+0.0182</i>	<i>+4.42/+0.0401</i>	<i>+0.72/+0.0427</i>	<i>+0.50/+0.0125</i>	<i>+2.78/+0.0598</i>

Table 1 and Figure 3 illustrate DAIR’s performance across six common degradations. Achieving the highest average **PSNR (28.15)** and **SSIM (0.8829)**, DAIR delivers significant improvements, including **+5.64 PSNR** and **+0.0758 SSIM** in desnowing, and **+1.54 PSNR** and **+0.0481 SSIM** in lowlight enhancement. Despite requiring only **45G FLOPs**, DAIR outperforms computationally intensive methods like ADAIR Cui et al. (2024) (**147G FLOPs**) while operating without MP, ensuring scalability and adaptability. By leveraging degradation-aware latent priors, DAIR generates robust, high-quality restorations across diverse degradation types, making it ideal for real-world applications like autonomous systems and healthcare imaging.

<sup>1</sup>Computed on  $256 \times 256$  images.

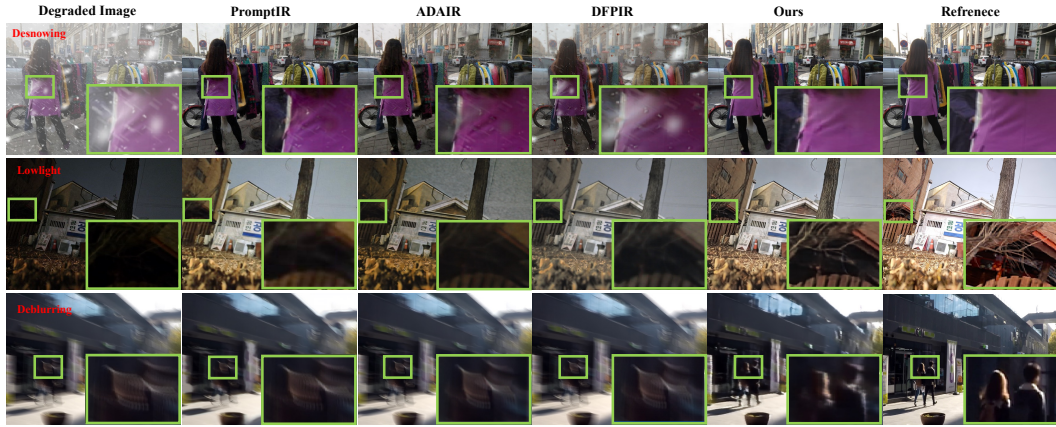


Figure 3: Visual comparison for six common degradation settings. The proposed method produces consistent and plausible images compared to the existing methods.

#### 4.2.2 SINGLE-TASK EVALUATION: LLIE AND DESNOWING

Table 2: Performance comparison on desnowing and LLIE tasks. Best results in **bold red**, second best underlined. Improvement over the best-performing method highlighted in **blue**.

(a) Desnowing		(b) Low-light enhancement	
Method	PSNR↑/SSIM↑	Method	PSNR↑/SSIM↑
HDCWNet Zhu et al. (2021)	<u>29.25</u> /0.9171	RetinexNet Wei et al. (2018)	14.19/0.5183
TransWeather Valanarasu et al. (2022)	<u>23.30</u> /0.7631	Diff-Retinex Yi et al. (2023)	<u>15.38</u> /0.5038
Uformer Wang et al. (2022)	<u>28.86</u> /0.9324	Uformer Wang et al. (2022)	13.05/0.5716
Restormer Zamir et al. (2022)	<u>23.21</u> /0.8686	Restormer Zamir et al. (2022)	<u>15.78</u> /0.6184
ADAIR Cui et al. (2024)	28.31/0.9300	ADAIR Cui et al. (2024)	15.19/0.6094
<b>DAIR (Ours)</b>	<b>32.75</b> / <b>0.9632</b>	<b>DAIR (Ours)</b>	<b>16.30</b> / <b>0.6634</b>
<i>Improvement</i>	<i>+3.50/+0.0308</i>	<i>Improvement</i>	<i>+0.52/+0.0450</i>

We evaluated DAIR on single restoration tasks to demonstrate its adaptability. Table 2 shows DAIR achieves **32.75 PSNR / 0.9632 SSIM** for desnowing, outperforming HDCWNet Zhu et al. (2021) by **+3.50 PSNR / +0.0308 SSIM**. For LLIE, DAIR achieves **16.30 PSNR / 0.6634 SSIM**, improving upon Restormer Zamir et al. (2022) by **+0.52 PSNR / +0.0450 SSIM**. By leveraging degradation-aware latent priors, DAIR can also adapt to varying degradation types without external MP.

#### 4.3 RESULTS ON COMPOUND DEGRADATION

Table 3: Performance comparison across five compound degradation. Best results in **bold red**, second best underlined. Improvement over the best-performing method highlighted in **blue**.

Method	Haze + Rain PSNR↑/SSIM↑	Low + Haze PSNR↑/SSIM↑	Low + Haze + Rain PSNR↑/SSIM↑	Low + Haze + Snow PSNR↑/SSIM↑	Low + Snow PSNR↑/SSIM↑	Average PSNR↑/SSIM↑
Uformer Wang et al. (2022)	22.49/0.8889	21.37/0.8252	20.61/0.7838	18.64/0.6802	20.31/0.7150	20.68/0.7786
Restormer Zamir et al. (2022)	<u>23.57</u> /0.8825	<u>21.44</u> /0.7753	20.53/0.7265	18.46/0.6494	19.97/0.6664	20.79/0.7400
AIRNet Li et al. (2022)	18.58/0.7977	11.73/0.6905	13.58/0.6320	12.87/0.5989	13.76/0.5759	14.10/0.6572
PromptIR Vaishnav et al. (2023)	21.78/0.8818	20.63/0.8231	19.83/0.7705	18.42/0.6801	20.74/0.7070	20.28/0.7725
DiffUIR Zheng et al. (2024)	18.42/0.8022	14.28/0.7150	15.79/0.6568	15.33/0.6238	12.60/0.6292	15.28/0.6854
ADAIR Cui et al. (2024)	<u>23.51</u> /0.8966	<u>22.78</u> /0.8420	<u>21.06</u> /0.7908	<u>20.46</u> /0.7229	<u>21.35</u> /0.7215	<u>21.83</u> /0.7948
DFPIR Tian et al. (2025a)	20.81/0.8308	19.01/0.7784	18.82/0.7139	15.58/0.6307	19.70/0.6402	18.78/0.7188
<b>DAIR (Ours)</b>	<b>25.25</b> / <b>0.9259</b>	<b>23.15</b> / <b>0.8541</b>	<b>22.03</b> / <b>0.8200</b>	<b>20.81</b> / <b>0.7613</b>	<b>21.79</b> / <b>0.7772</b>	<b>22.61</b> / <b>0.8277</b>
<i>Improvement</i>	<i>+1.68/+0.0293</i>	<i>+0.37/+0.0121</i>	<i>+0.97/+0.0292</i>	<i>+0.35/+0.0384</i>	<i>+0.44/+0.0557</i>	<i>+0.78/+0.0329</i>

We evaluated DAIR on compound degradation scenarios. As shown in Table 3, DAIR achieves the highest average **PSNR of 22.61** and **SSIM of 0.8277**, outperforming the next-best method (ADAIR Cui et al. (2024)) by **+0.78 PSNR / +0.0329 SSIM**. Notable improvements include "Haze + Rain" (**+1.68 PSNR / +0.0293 SSIM**) and "Low + Snow" (**+0.44 PSNR / +0.0557 SSIM**). DAIR effectively restores overlapping degradations, demonstrating robust performance across complex scenarios. Fig. 4 highlights DAIR's superior visual quality, producing artifact-free, natural images.

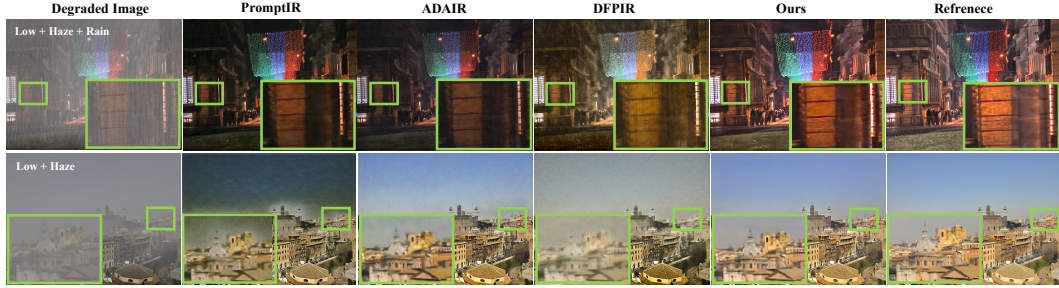


Figure 4: Visual comparison for five compound degradations. The proposed DAIR can handle compound degradation and produce visually pleasing images.

#### 4.4 LATENT PRIOR GUIDED UNSEEN TASK RESTORATION

The primary motivation for leveraging latent priors is to address unknown degradations while maintaining a clear distinction from known degradations. Fig. 5 highlights the restoration of unknown compound degradations, comparing DAIR with SOTA methods. Our approach effectively handles these degradations, as demonstrated by t-SNE visualization in Fig. 5 (b). Table 4 summarizes the results, showing that our method achieves notable improvements over existing approaches, with average gains of **+1.47 dB PSNR** and **+0.0412 SSIM** for unseen degradations.

Table 4: Performance comparison on unknown compound degradations. Best results in **bold red**, second best underlined. Improvement over the best-performing method highlighted in **blue**.

Method	Haze + Snow PSNR↑/SSIM↑	Low + Rain PSNR↑/SSIM↑	Average PSNR↑/SSIM↑
ADAIR Cui et al. (2024)	16.07/0.8130	21.67/0.7877	18.87/0.8003
PromptIR Vaishnav et al. (2023)	17.84/0.8032	21.15/0.7752	<u>19.50/0.7892</u>
DFPIR Tian et al. (2025a)	14.50/0.7577	21.52/0.7021	18.01/0.7299
<b>DAIR (Ours)</b> <i>Improvement</i>	<b>18.65/0.8531</b> <b>+0.81/+0.0499</b>	<b>23.29/0.8299</b> <b>+1.62+0.0422</b>	<b>20.97/0.8415</b> <b>+1.47+0.0523</b>

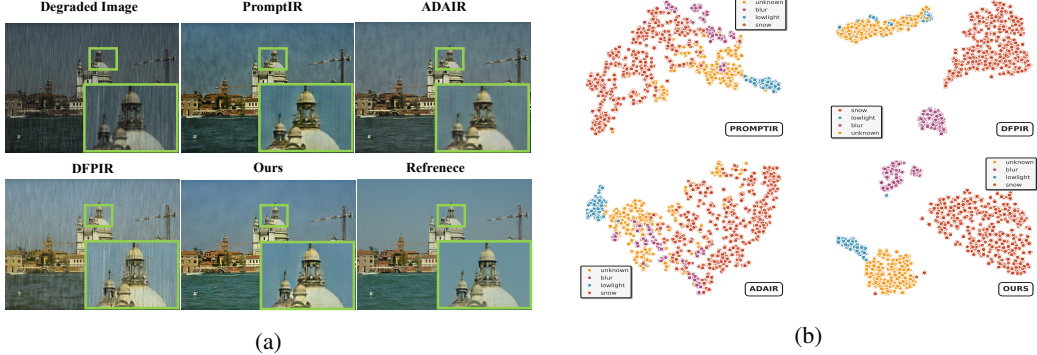


Figure 5: DAIR performance on unseen tasks: (a) Visual results for unseen compound degradation (low-light + rain); (b) t-SNE embeddings showing separation of unseen and known degradations.

#### 4.5 DEGRADATION MAP

Our proposed DM effectively learns spatially correlated regions, enabling the decoder to focus on "where" to reconstruct the degraded image. As shown in Fig. 6, the comparison with traditional skip connections highlights that our learnable approach precisely identifies affected areas and significantly outperforms conventional methods.

#### 4.6 RESTORATION WITH 3WD

We evaluate DAIR with 3WD against self-attention (SA) Vaswani et al. (2017) and cross-attention (CA) Vaswani et al. (2017) base-



Figure 6: Visualization and restoration with the proposed DM.

lines. As shown in Table 5, DAIR with 3WD consistently outperforms both baselines, achieving average improvements of **+7.72 dB PSNR** and **+0.2605 SSIM**, with significant gains in desnowing (**+11.89 dB**) and denoising (**+8.24 dB**). Additionally, DAIR operates with linear complexity  $O(d^2 \times H \times W)$  compared to the baselines’ quadratic  $O(d \times H^2 \times W^2)$ , delivering **85-257x speedup** and **76-89% memory reduction** while answering our reasoning cues.

Table 5: Performance comparison of proposed 3WD restoration with existing attention mechanism. Best results in **bold red**, second best underlined. Improvement over the best performing method highlighted in **blue**.

Method	Complexity (Speedup)	Denoising PSNR↑/SSIM↑	Desnowing PSNR↑/SSIM↑	Deraining PSNR↑/SSIM↑	Lowlight PSNR↑/SSIM↑	Average PSNR↑/SSIM↑
DAIR + SA Vaswani et al. (2017)	$O(H^2W^2)$	18.90/0.6213	19.70/0.6738	22.94/0.6541	15.16/0.4348	19.18/0.5960
DAIR + CA Vaswani et al. (2017)	$O(H^2W^2)$	20.87/0.6290	16.07/0.6469	20.90/0.6448	13.00/0.3854	17.71/0.5765
<b>DAIR + 3WD (Ours)</b>	<b><math>O(HW)</math></b>	<b>29.11/0.8971</b>	<b>31.59/0.9581</b>	<b>30.21/0.9070</b>	<b>16.68/0.6638</b>	<b>26.90/0.8565</b>
<i>Improvement</i>	Linear scaling	+8.24/+0.2681	+11.89/+0.2843	+7.27/+0.2529	+1.52/+0.2290	+7.72/+0.2605

#### 4.7 ABLATION STUDY

We conducted an ablation study to evaluate DAIR’s key components: Latent Priors Encoding (LPE) (“which”), Degradation Map (DM) (“where”), Latent fusion (LF) (“what”), and Restoration Block (3WD). As shown in Table 6, the inclusion of the proposed component progressively enhances performance, with DAIR achieving the highest average **PSNR of 26.90** and **SSIM of 0.8565**. Notably, removing Latent Priors results in significantly worse performance (**-4.23 PSNR / -0.0876 SSIM**), highlighting its critical role in capturing detailed degradation descriptions, subsequently guiding the model in effectively segregating different types of degradations.

Table 6: Ablation study on key components. Tick (✓) indicates the component is used, cross (✗) indicates not used. Best results in **bold red**.

Method	LP	LF	DM	3WD	Denoise PSNR↑/SSIM↑	Desnowing PSNR↑/SSIM↑	Derain PSNR↑/SSIM↑	Lowlight PSNR↑/SSIM↑	Average PSNR↑/SSIM↑
Base Model	✗	✗	✗	✗	23.42/0.7237	20.76/0.7696	22.70/0.7698	13.99/0.5111	20.22/0.6936
Base + LP	✓	✗	✗	✗	24.50/0.7417	20.75/0.7783	22.46/0.7658	14.23/0.5240	20.49/0.7025
Base + LP + LF	✓	✓	✗	✗	25.83/0.7799	21.21/0.8014	22.23/0.7545	15.04/0.5474	21.08/0.7208
Base + LP + LF + DM	✓	✓	✓	✗	26.80/0.8158	21.97/0.8442	22.79/0.7614	15.52/0.5540	21.77/0.7439
DAIR w/o Latent Prior	✗	✗	✓	✓	26.07/0.8855	26.83/0.8306	22.76/0.7741	15.00/0.5853	22.67/0.7689
<b>DAIR</b>	<b>✓</b>	<b>✓</b>	<b>✓</b>	<b>✓</b>	<b>29.11/0.8971</b>	<b>31.59/0.9581</b>	<b>30.21/0.9070</b>	<b>16.68/0.6638</b>	<b>26.90/0.8565</b>
<i>Improvement</i>					+5.69/+0.1734	+10.83/+0.1885	+7.51/+0.1372	+2.69/+0.1527	+6.68/+0.1629

## 5 CONCLUSION

We propose DAIR, a unified framework for AIR that tackles the challenges of unknown and compound degradations by learning degradation characteristics directly from the degraded image itself, eliminating the need for manual text or visual prompts. Guided by a reasoning paradigm based on “which features to use, where to focus while restoring, and what to restore”, DAIR enables spatially adaptive restoration through a lightweight decoder that effectively integrates all prior information. Extensive experiments demonstrate that DAIR surpasses SOTA methods across six common and five compound degradation scenarios, while robustly handling unseen cases, highlighting its scalability and generalizability. Further details on implementation, analysis, unseen cases, downstream vision tasks, and additional results are provided in the appendix.

## REFERENCES

Abdulrahman Abdelhamed, Stephen Lin, and Michael S. Brown. A high-quality denoising dataset for smartphone cameras. In *Proceedings of the IEEE Conference on Computer Vision and Pattern Recognition (CVPR)*, pp. 1692–1700, 2018.

Eirikur Agustsson and Radu Timofte. Ntire 2017 challenge on single image super-resolution: Dataset and study. In *Proceedings of the IEEE Conference on Computer Vision and Pattern Recognition Workshops (CVPRW)*, pp. 126–135, 2017.

---

Tim Brooks, Aleksander Holynski, and Alexei A Efros. Instructpix2pix: Learning to follow image editing instructions. In *Proceedings of the IEEE/CVF conference on computer vision and pattern recognition*, pp. 18392–18402, 2023.

Yuanhao Cai, Hao Bian, Jing Lin, Haoqian Wang, Radu Timofte, and Yulun Zhang. Retinex-former: One-stage retinex-based transformer for low-light image enhancement. *arXiv preprint arXiv:2303.06705*, 2023.

Wei-Ting Chen, Hao-Yu Fang, Cheng-Lin Hsieh, Cheng-Che Tsai, I Chen, Jian-Jiun Ding, Sy-Yen Kuo, et al. All snow removed: Single image desnowing algorithm using hierarchical dual-tree complex wavelet representation and contradict channel loss. In *Proceedings of the IEEE/CVF international conference on computer vision*, pp. 4196–4205, 2021.

Sung-Jin Cho, Seo-Won Ji, Jun-Pyo Hong, Seung-Won Jung, and Sung-Jea Ko. Rethinking coarse-to-fine approach in single image deblurring. In *Proceedings of the IEEE/CVF international conference on computer vision*, pp. 4641–4650, 2021.

James W Cooley and John W Tukey. An algorithm for the machine calculation of complex fourier series. *Mathematics of computation*, 19(90):297–301, 1965.

Yuning Cui, Syed Waqas Zamir, Salman Khan, Alois Knoll, Mubarak Shah, and Fahad Shahbaz Khan. Adair: Adaptive all-in-one image restoration via frequency mining and modulation. *arXiv preprint arXiv:2403.14614*, 2024.

Hang Dong, Jinshan Pan, Lei Xiang, Zhe Hu, Xinyi Zhang, Fei Wang, and Ming-Hsuan Yang. Multi-scale boosted dehazing network with dense feature fusion. In *Proceedings of the IEEE/CVF conference on computer vision and pattern recognition*, pp. 2157–2167, 2020.

Xueyang Fu, Jianbin Huang, Delu Zeng, Yinghao Wang, Xinghao Ding, and John Paisley. Deep detail network for rain removal from single images. In *Proceedings of the IEEE Conference on Computer Vision and Pattern Recognition (CVPR)*, pp. 3855–3863, 2017.

Hu Gao, Jing Yang, Ying Zhang, Ning Wang, Jingfan Yang, and Depeng Dang. Prompt-based ingredient-oriented all-in-one image restoration. *IEEE Transactions on Circuits and Systems for Video Technology*, 34(10):9458–9471, 2024.

Shuai Guo et al. Letting go of self-domain awareness: Multi-source domain-adversarial generalization via dynamic domain-weighted contrastive transfer learning. In *Frontiers in Artificial Intelligence and Applications*, pp. 450–461. IOS Press, 2023. doi: 10.3233/FAIA230450.

Yu Guo, Yuan Gao, Yuxu Lu, Huilin Zhu, Ryan Wen Liu, and Shengfeng He. Onerestore: A universal restoration framework for composite degradation. In *European conference on computer vision*, pp. 255–272. Springer, 2024.

Kaiming He, Xiangyu Zhang, Shaoqing Ren, and Jian Sun. Deep residual learning for image recognition. In *Proceedings of the IEEE Conference on Computer Vision and Pattern Recognition (CVPR)*, pp. 770–778, 2016.

Jie Hu, Li Shen, and Gang Sun. Squeeze-and-excitation networks. In *Proceedings of the IEEE conference on computer vision and pattern recognition*, pp. 7132–7141, 2018.

Junjun Jiang, Zengyuan Zuo, Gang Wu, Kui Jiang, and Xianming Liu. A survey on all-in-one image restoration: Taxonomy, evaluation and future trends. *IEEE Transactions on Pattern Analysis and Machine Intelligence*, 2025.

Kui Jiang, Zhongyuan Wang, Peng Yi, Chen Chen, Baojin Huang, Yimin Luo, Jiayi Ma, and Junjun Jiang. Multi-scale progressive fusion network for single image deraining. In *Proceedings of the IEEE/CVF conference on computer vision and pattern recognition*, pp. 8346–8355, 2020.

Jun-Cheng Ke, Weijie Wang, and Tomas Pfister. Musiq: Multi-scale image quality. In *Proceedings of the IEEE/CVF International Conference on Computer Vision (ICCV)*, pp. 5148–5157, 2021.

---

Jiwon Kim, Jung Kwon Lee, and Kyoung Mu Lee. Accurate image super-resolution using very deep convolutional networks. In *Proceedings of the IEEE Conference on Computer Vision and Pattern Recognition (CVPR)*, pp. 1646–1654, 2016.

Diederik P Kingma and Max Welling. Auto-encoding variational bayes. *arXiv preprint arXiv:1312.6114*, 2013.

Diederik P Kingma and Max Welling. Auto-encoding variational bayes. In *International Conference on Learning Representations (ICLR)*, 2014. URL <https://arxiv.org/abs/1312.6114>.

Solomon Kullback and Richard A. Leibler. On information and sufficiency. *The Annals of Mathematical Statistics*, 22(1):79–86, 1951.

Boyi Li, Wenqi Ren, Dengpan Fu, Dacheng Tao, Dan Feng, Wenjun Zeng, and Zhangyang Wang. Benchmarking single-image dehazing and beyond. *IEEE transactions on image processing*, 28(1):492–505, 2018.

Boyuan Li, Xiao Liu, Peng Hu, Zhongqin Wu, Jiancheng Lv, and Xi Peng. All-in-one image restoration for unknown corruption. In *Proceedings of the IEEE/CVF conference on computer vision and pattern recognition*, pp. 17452–17462, 2022.

Rui Li, Qian Wu, Zongyuan Lin, Hao Liu, and Jie Zhou. Desnownet: Context-aware deep network for snow removal. *IEEE Transactions on Image Processing*, 29:5488–5502, 2020.

Yidi Liu, Dong Li, Xueyang Fu, Xin Lu, Jie Huang, and Zheng-Jun Zha. Uhd-processer: Unified uhd image restoration with progressive frequency learning and degradation-aware prompts. In *Proceedings of the Computer Vision and Pattern Recognition Conference*, pp. 23121–23130, 2025.

Xiaoqiao Mao, Chunhua Shen, and Yu-Bin Yang. Image restoration using very deep convolutional encoder-decoder networks with symmetric skip connections. *Advances in neural information processing systems*, 29, 2016.

David Martin, Charless Fowlkes, Doron Tal, and Jitendra Malik. A database of human segmented natural images and its application to evaluating segmentation algorithms and measuring ecological statistics. *Proceedings of the IEEE International Conference on Computer Vision (ICCV)*, 2:416–423, 2001.

Anish Mittal, Rajiv Soundararajan, and Alan C. Bovik. Making a “completely blind” image quality analyzer. *IEEE Signal Processing Letters*, 20(3):209–212, 2013.

Seungjun Nah, Tae Hyun Kim, and Kyoung Mu Lee. Deep multi-scale convolutional neural network for dynamic scene deblurring. In *Proceedings of the IEEE Conference on Computer Vision and Pattern Recognition*, 2017.

Tongyao Pang, Huan Zheng, Yuhui Quan, and Hui Ji. Recorrupted-to-recorrupted: Unsupervised deep learning for image denoising. In *Proceedings of the IEEE/CVF conference on computer vision and pattern recognition*, pp. 2043–2052, 2021.

Yuhuan Peng and Pamela C. Cosman. An underwater image enhancement benchmark dataset and beyond. *IEEE Access*, 7:123488–123501, 2019.

Ethan Perez, Florian Strub, Harm De Vries, Vincent Dumoulin, and Aaron Courville. Film: Visual reasoning with a general conditioning layer. In *Proceedings of the AAAI conference on artificial intelligence*, volume 32, 2018.

Xu Qin, Zhilin Wang, Yuanchao Bai, Xiaodong Xie, and Huizhu Jia. Ffa-net: Feature fusion attention network for single image dehazing. In *Proceedings of the AAAI conference on artificial intelligence*, volume 34, pp. 11908–11915, 2020.

Alec Radford, Jong Wook Kim, Rob Hallacy, Aditya Ramesh, Gabriel Goh, Sandhini Agarwal, Girish Sastry, Amanda Askell, Pamela Mishkin, Jack Clark, Scott Krueger, and Ilya Sutskever. Learning transferable visual models from natural language supervision. In *Proceedings of the 38th International Conference on Machine Learning (ICML)*, pp. 8748–8763. PMLR, 2021.

---

Dongwei Ren, Wangmeng Zuo, Qinghua Hu, Pengfei Zhu, and Deyu Meng. Progressive image deraining networks: A better and simpler baseline. In *Proceedings of the IEEE/CVF conference on computer vision and pattern recognition*, pp. 3937–3946, 2019.

Amirreza Rezvantalab, Habib Safigholi, and Somayeh Karimijeshni. Dermatologist level dermoscopy skin cancer classification using different deep learning convolutional neural networks algorithms. *arXiv preprint arXiv:1810.10348*, 2018.

Robin Rombach, Andreas Blattmann, Dominik Lorenz, Patrick Esser, and Björn Ommer. High-resolution image synthesis with latent diffusion models. In *Proceedings of the IEEE/CVF Conference on Computer Vision and Pattern Recognition (CVPR)*, pp. 10684–10695, 2022.

S M A Sharif, Abdur Rehman, Zain Ul Abidin, Fayaz Ali Dharejo, Radu Timofte, and Rizwan Ali Naqvi. Illuminating darkness: Learning to enhance low-light images in-the-wild, 2025. URL <https://arxiv.org/abs/2503.06898>.

SMA Sharif, Rizwan Ali Naqvi, Mithun Biswas, and Woong-Kee Loh. Deep perceptual enhancement for medical image analysis. *IEEE Journal of Biomedical and Health Informatics*, 26(10):4826–4836, 2022.

Alvy Ray Smith. Color gamut transform pairs. *SIGGRAPH '78: Proceedings of the 5th annual conference on Computer graphics and interactive techniques*, pp. 12–19, 1978.

Xiangpeng Tian, Xiangyu Liao, Xiao Liu, Meng Li, and Chao Ren. Degradation-aware feature perturbation for all-in-one image restoration. In *Proceedings of the Computer Vision and Pattern Recognition Conference*, pp. 28165–28175, 2025a.

Yunjie Tian, Qixiang Ye, and David Doermann. Yolov12: Attention-centric real-time object detectors. *arXiv preprint arXiv:2502.12524*, 2025b.

Mathias Uhlen, Per Oksvold, Linn Fagerberg, Emma Lundberg, Kalle Jonasson, Mattias Forsberg, Martin Zwahlen, Caroline Kampf, Kenneth Wester, Sophia Hober, et al. Towards a knowledge-based human protein atlas. *Nature biotechnology*, 28(12):1248–1250, 2010.

P Vaishnav, Z Syed Waqas, K Salman, and K Fahad Shahbaz. Promptir: Prompting for all-in-one blind image restoration. *arXiv preprint arXiv:2306.13090*, 2023.

Jeya Maria Jose Valanarasu, Rajeev Yasarla, and Vishal M Patel. Transweather: Transformer-based restoration of images degraded by adverse weather conditions. In *Proceedings of the IEEE/CVF conference on computer vision and pattern recognition*, pp. 2353–2363, 2022.

Ashish Vaswani, Noam Shazeer, Niki Parmar, Jakob Uszkoreit, Llion Jones, Aidan N Gomez, Łukasz Kaiser, and Illia Polosukhin. Attention is all you need. *Advances in neural information processing systems*, 30, 2017.

Zhendong Wang, Xiaodong Cun, Jianmin Bao, Wengang Zhou, Jianzhuang Liu, and Houqiang Li. Uformer: A general u-shaped transformer for image restoration. In *Proceedings of the IEEE/CVF conference on computer vision and pattern recognition*, pp. 17683–17693, 2022.

Chen Wei, Wenjing Wang, Wenhan Yang, and Jiaying Liu. Deep retinex decomposition for low-light enhancement. In *Proceedings of the British Machine Vision Conference (BMVC)*, 2018.

Qingsen Yan, Yixu Feng, Cheng Zhang, Guansong Pang, Kangbiao Shi, Peng Wu, Wei Dong, Jin- qiu Sun, and Yanning Zhang. Hvi: A new color space for low-light image enhancement. In *Proceedings of the Computer Vision and Pattern Recognition Conference*, pp. 5678–5687, 2025.

Xunpeng Yi, Han Xu, Hao Zhang, Linfeng Tang, and Jiayi Ma. Diff-retinex: Rethinking low-light image enhancement with a generative diffusion model. In *Proceedings of the IEEE/CVF international conference on computer vision*, pp. 12302–12311, 2023.

Syed Waqas Zamir, Aditya Arora, Salman Khan, Munawar Hayat, Fahad Shahbaz Khan, and Ming- Hsuan Yang. Restormer: Efficient transformer for high-resolution image restoration. In *Proceedings of the IEEE/CVF Conference on Computer Vision and Pattern Recognition*, pp. 5728–5739, 2022.

---

Kai Zhang, Wangmeng Zuo, Yunjin Chen, Deyu Meng, and Lei Zhang. Beyond a gaussian denoiser: Residual learning of deep cnn for image denoising. *IEEE transactions on image processing*, 26(7):3142–3155, 2017.

Kai Zhang, Wangmeng Zuo, and Lei Zhang. Ffdnet: Toward a fast and flexible solution for cnn-based image denoising. *IEEE Transactions on Image Processing*, 27(9):4608–4622, 2018a.

Richard Zhang, Phillip Isola, Alexei A. Efros, Eli Shechtman, and Oliver Wang. The unreasonable effectiveness of deep features as a perceptual metric. *Proceedings of the IEEE Conference on Computer Vision and Pattern Recognition (CVPR)*, pp. 586–595, 2018b.

Dian Zheng, Xiao-Ming Wu, Shuzhou Yang, Jian Zhang, Jian-Fang Hu, and Wei-Shi Zheng. Selective hourglass mapping for universal image restoration based on diffusion model. In *Proceedings of the IEEE/CVF conference on computer vision and pattern recognition*, pp. 25445–25455, 2024.

Lei Zhu, Mingfu Wen, Wenhao Li, Yuan Wang, Huazhu Fu, Dong Xu, and Xinghao Ding. Hierarchical dense connection and wavelet network for single image deraining. *IEEE Transactions on Image Processing*, 30:2039–2053, 2021.

## APPENDIX

### A NETWORK DETAILS

#### A.1 MOTIVATION

A major challenge in all-in-one image restoration is encoding degradation-specific information in a compact yet generalizable form while recovering clean images  $\mathbf{I}$  from degraded observations  $\mathbf{I}_{deg} = \mathcal{D}_R(\mathbf{I}) + \epsilon$ , where degradations  $\mathcal{D}_R$  may arise from diverse sources. Current methods rely on explicit degradation cues, limiting their ability to handle unknown or compositional degradations.

From an information-theoretic perspective, effective restoration requires learning the conditional distribution  $p(\mathbf{I}|\mathbf{I}_{deg})$  by disentangling degradation-specific information from content-preserving features. We model this through a variational framework where degradation characteristics are encoded in latent variable  $\mathbf{z} \sim p(\mathbf{z}|\mathbf{I}_{deg})$ . The VAE objective  $\mathcal{L} = -\mathbb{E}_{q_\phi(\mathbf{z}|\mathbf{I}_{deg})}[\log p_\theta(\mathbf{I}|\mathbf{z}, \mathbf{I}_{deg})] + \beta \cdot \text{KL}(q_\phi(\mathbf{z}|\mathbf{I}_{deg})||p(\mathbf{z}))$  learns meaningful degradation representations while ensuring generalization through prior regularization. Degradations exhibit domain-specific characteristics: let  $\mathbf{I}_{deg} = [L, C]$  where  $L$  represents luminance and  $C$  chrominance components. Structural degradations primarily affect  $L$  while color distortions manifest in  $C$ . Factorizing the posterior as  $q_\phi(\mathbf{z}|\mathbf{I}_{deg}) = q_{\phi_L}(\mathbf{z}_L|L) \cdot q_{\phi_C}(\mathbf{z}_C|C)$  enables specialized degradation modeling, reducing cross-domain interference and improving restoration through  $p_\theta(\mathbf{I}|\mathbf{z}_L, \mathbf{z}_C, \mathbf{I}_{deg})$ . We propose a hybrid VAE with separate LC encoders that automatically infers continuous degradation latent without explicit MP.

#### A.2 VAE DESIGN

**Architecture.** To effectively integrate the VAE into our framework, we design a hybrid U-Net encoder-decoder with multi-head self-attention Tian et al. (2025a) at the bottleneck. In particular, both the hybrid VAE and the reconstruction network incorporate the same spatial feature dimensions, enabling seamless interaction between latent representations and restoration features. The encoder progressively downsamples RGB images through four stages with channel dimensions [40, 80, 160, 320] using 3x3 convolutions (stride=2 for downsampling, padding=1). Each stage contains a Residual Attention Block He et al. (2016) combining spatial convolutions with channel attention Hu et al. (2018) (reduction ratio 8):

$$\text{ResAttn}(\mathbf{f}) = \mathbf{f} + \text{Conv}_{3 \times 3}(\text{ReLU}(\text{Conv}_{3 \times 3}(\mathbf{f}))) \odot \sigma(\text{Conv}_{1 \times 1}(\text{GAP}(\mathbf{f}))) \quad (11)$$

The bottleneck applies 2 layers of Multi-Head Self-Attention (4 heads,  $d_k = 80$ ) to the deepest features  $\mathbf{x}_3 \in \mathbb{R}^{H/8 \times W/8 \times 320}$ .

$$\mathbf{Q}, \mathbf{K}, \mathbf{V} = \mathbf{x}_3 \mathbf{W}^Q, \mathbf{x}_3 \mathbf{W}^K, \mathbf{x}_3 \mathbf{W}^V \quad (12)$$

$$\text{MHSA}(\mathbf{x}_3) = \text{softmax} \left( \frac{\mathbf{Q}\mathbf{K}^T}{\sqrt{80}} \right) \mathbf{V} \quad (13)$$

Latent parameters are computed as  $\mu, \log \sigma^2 = \text{Conv}_{1 \times 1}(\text{MHSA}^2(\mathbf{x}_3))$  with latent dimension 320 and reparameterization  $\mathbf{z} = \mu + \sigma \odot \epsilon$ . The decoder mirrors the encoder using transposed convolutions (stride=2) and identical ResAttn blocks, producing reconstructions  $\hat{\mathbf{I}}_{deg} = \tanh(\text{Conv}(\text{Decoder}(\mathbf{z})))$ .

**Objective Function.** We train the complete VAE architecture using a multi-component loss function:

$$\mathcal{L}_{\text{VAE}} = \mathcal{L}_{\text{recon}} + \beta \mathcal{L}_{\text{KL}} + \lambda_{\text{con}} \mathcal{L}_{\text{SupCon}} \quad (14)$$

where  $\beta$  and  $\lambda_{\text{con}}$  are balancing hyperparameters for different loss components to stabilize VAE training. We set  $\beta = 0.3$  to provide strong KL regularization ensuring proper latent space structure, and  $\lambda_{\text{con}} = 0.01$  to enable weak supervision for degradation separation at the deepest encoder level (pre-latent space).

The reconstruction loss employs L1 distance to ensure pixel-level fidelity:

$$\mathcal{L}_{\text{recon}} = \|\mathbf{I}_{deg} - \hat{\mathbf{I}}_{deg}\|_1 \quad (15)$$

where  $\mathbf{I}_{deg}$  is the input degraded image and  $\hat{\mathbf{I}}_{deg} = D_{\theta}(\mathbf{z})$  is the reconstructed output from the decoder.

The KL divergence Kullback & Leibler (1951) term regularizes the latent distribution:

$$\mathcal{L}_{\text{KL}} = \text{KL}(q_{\phi}(\mathbf{z}|\mathbf{I}_{deg}) \parallel \mathcal{N}(\mathbf{0}, \mathbf{I})) \quad (16)$$

This loss term encourages the learned latent distribution  $q_{\phi}(\mathbf{z}|\mathbf{I}_{deg})$  to be close to a standard normal distribution  $\mathcal{N}(\mathbf{0}, \mathbf{I})$ , ensuring that the latent space has good sampling properties and prevents overfitting.

To encourage discriminative latent representations, we incorporate weakly Supervised Contrastive Learning Guo et al. (2023) on the spatially-pooled encoder:

$$\mathcal{L}_{\text{SupCon}} = - \sum_i \log \frac{\sum_{j \in P_i} \exp(\mathbf{z}_i \cdot \mathbf{z}_j / \tau)}{\sum_{k \neq i} \exp(\mathbf{z}_i \cdot \mathbf{z}_k / \tau)} \quad (17)$$

where  $\mathbf{z}_i$  are the normalized features,  $P_i$  represents samples with the same degradation label as sample  $i$ , and  $\tau = 0.1$  is the temperature parameter. This loss pulls together samples from the same degradation category while pushing apart samples from different categories in the latent space, encouraging the encoder to learn discriminative representations for different types of image degradations.

### A.3 DAIR DETAILS

**Architecture.** We employ a dual-branch encoder with separate LC processing. RGB inputs are decomposed as  $L = 0.299R + 0.587G + 0.114B$ ,  $C = RGB - L$ . Illumination and chrominance estimators utilize depthwise convolutions (kernel size=5, groups=4) to generate adaptive maps. Input embeddings are computed as  $\mathbf{f}_{lum} = \text{LeakyReLU}(\text{Conv}_{3 \times 3}(\mathbf{I}_{deg} \cdot \text{IllumMap} + \mathbf{I}_{deg}))$  and  $\mathbf{f}_{chrom} = \text{LeakyReLU}(\text{Conv}_{3 \times 3}(\mathbf{I}_{deg} \cdot \text{ChromMap} + \mathbf{I}_{deg}))$ .

The encoder processes four levels with channel dimensions progressing as  $40 \rightarrow 80 \rightarrow 160 \rightarrow 320$  for both LC branches. Downsampling uses  $\text{Conv}_{3 \times 3}$  with stride=2 and padding=1, followed by LeakyReLU (slope=0.1). The decoder mirrors this structure using  $\text{ConvTranspose}_{2 \times 2}$  (stride=2) for upsampling  $320 \rightarrow 160 \rightarrow 80 \rightarrow 40$ . Final reconstruction applies  $\text{Conv}_{3 \times 3}(\text{decoder\_out}) + \mathbf{I}_{deg}$  with tanh activation. All convolutions use padding=1 for embedding layers and one attention block per level.

---

**Objective Function.** The restoration network loss combines L1 reconstruction loss with SSIM-based perceptual loss:

$$\mathcal{L}_{\text{recon}} = \|\hat{\mathbf{I}} - \mathbf{I}\|_1 + \lambda_{\text{ssim}} \left( 1 - \text{SSIM} \left( \frac{\hat{\mathbf{I}} + 1}{2}, \frac{\mathbf{I} + 1}{2} \right) \right) \quad (18)$$

where images are normalized from  $[-1, 1]$  to  $[0, 1]$  range for SSIM computation, and  $\lambda_{\text{ssim}} = 1.0$ . The L1 loss ensures pixel-level fidelity while SSIM preserves perceptual quality and structural information. This combination effectively handles both fine-grained details and global image structure during restoration.

#### A.4 TRAINING DETAILS

Algorithm 1 details the complete training procedure. Notably, the VAE is trained only once using known degradation types, and the same pre-trained weights are utilized across all experiments, including single-task restoration, unseen degradation scenarios, and ablation studies, demonstrating the framework’s practical versatility in handling multi-degradation restoration tasks.

---

#### Algorithm 1 DAIR training for AIR

---

**Require:** Degraded images  $\{\mathbf{I}_{\text{deg},i}\}$ , clean images  $\{\mathbf{I}_i\}$ , labels  $\{y_i\}$   
**Ensure:** Trained VAE  $\theta_{\text{VAE}}$ , restoration network  $\theta_{\text{REST}}$

- 1: Initialize HybridVAE( $\theta_{\text{VAE}}$ ), RestNet( $\theta_{\text{REST}}$ )
- 2: Set  $T_1 = 300\text{K}$ ,  $T_2 = 100\text{K}$ ,  $\beta_{\text{max}} = 0.3$ ,  $\lambda_{\text{con}} = 0.01$
- 3: **Phase 1: VAE Pretraining**
- 4: **for**  $t = 1$  to  $T_1$  **do**
- 5:      $\hat{\mathbf{I}}_{\text{deg}}, \boldsymbol{\mu}, \log \boldsymbol{\sigma}^2, \mathbf{x}_0, \mathbf{x}_1, \mathbf{x}_2, \mathbf{x}_3 \leftarrow \text{VAE}(\mathbf{I}_{\text{deg}})$
- 6:      $\hat{\mathbf{z}}_3 \leftarrow \text{L2Norm}(\text{GAP}(\mathbf{x}_3))$  {Contrastive features}
- 7:      $\mathcal{L}_{\text{recon}} = \|\hat{\mathbf{I}}_{\text{deg}} - \mathbf{I}_{\text{deg}}\|_1$
- 8:      $\mathcal{L}_{\text{KL}} = -\frac{1}{2} \sum (1 + \log \boldsymbol{\sigma}^2 - \boldsymbol{\mu}^2 - \boldsymbol{\sigma}^2)$
- 9:      $\mathcal{L}_{\text{SupCon}} = \text{SupConLoss}(\hat{\mathbf{z}}_3, y)$
- 10:     $\beta(t) = \min(\beta_{\text{max}}, \beta_{\text{max}} \cdot t/T_1)$  {KL annealing}
- 11:     $\mathcal{L}_{\text{VAE}} = \mathcal{L}_{\text{recon}} + \beta(t) \mathcal{L}_{\text{KL}} + \lambda_{\text{con}} \mathcal{L}_{\text{SupCon}}$
- 12:    Update  $\theta_{\text{VAE}}$  via  $\nabla_{\theta_{\text{VAE}}} \mathcal{L}_{\text{VAE}}$
- 13: **end for**
- 14: **Phase 2: Restoration Network Training**
- 15: Freeze( $\theta_{\text{VAE}}$ ) {Fix VAE parameters}
- 16: **for**  $t = T_1 + 1$  to  $T_1 + T_2$  **do**
- 17:      $\boldsymbol{\mu}, \mathbf{x}_0, \mathbf{x}_1, \mathbf{x}_2, \mathbf{x}_3 \leftarrow \text{VAE}(\mathbf{I}_{\text{deg}})$  {No gradients}
- 18:      $\hat{\mathbf{I}} \leftarrow \text{RestNet}(\mathbf{I}_{\text{deg}}, \mathbf{x}_0, \mathbf{x}_1, \mathbf{x}_2, \mathbf{x}_3, \boldsymbol{\mu})$
- 19:      $\mathcal{L}_{\text{recon}} = \|\hat{\mathbf{I}} - \mathbf{I}\|_1 + (1 - \text{SSIM}(\hat{\mathbf{I}}, \mathbf{I}))$
- 20:    Update  $\theta_{\text{REST}}$  via  $\nabla_{\theta_{\text{REST}}} \mathcal{L}_{\text{recon}}$
- 21: **end for**
- 22: **return**  $\theta_{\text{VAE}}, \theta_{\text{REST}}$

---

## B ADDITIONAL EXPERIMENTAL RESULTS

### B.1 QUANTITATIVE COMPARISON

#### B.1.1 LOW-LIGHT

We utilize the LSD dataset Sharif et al. (2025), collected in uncontrolled low-light settings, offering diverse indoor and outdoor scenes under varying conditions. Table 7 compares image restoration methods across extreme lowlight (under 50 Lux) and lowlight scenarios (50-200 lux), divided into indoor and outdoor subsets, using PSNR and SSIM metrics. Our method, DAIR, consistently outperforms others, with the best results highlighted in bold red and the second-best underlined. DAIR

achieves significant gains, improving up to +2.64 PSNR and +0.0737 SSIM in extreme lowlight, showcasing its robustness and superior generalization in challenging conditions.

Table 7: Performance comparison across lighting conditions. Best results in **bold red**, second best underlined.

Method	Extreme Lowlight			Lowlight	
	Indoor	Outdoor	PSNR↑/SSIM↑	Indoor	Outdoor
Uformer Wang et al. (2022)	11.98/0.5278	13.24/0.4628	<u>10.39/0.5535</u>	12.79/0.4145	
Restormer Zamir et al. (2022)	<u>14.99/0.6343</u>	<u>16.35/0.5828</u>	<u>16.07/0.7121</u>	<u>13.90/0.5429</u>	
AIRNet Li et al. (2022)	8.51/0.3678	9.80/0.3248	8.13/0.4585	9.05/0.3107	
PromptIR Vaishnav et al. (2023)	14.74/0.5902	16.10/0.5038	14.59/0.6404	13.48/0.4154	
DiffUIR Zheng et al. (2024)	9.77/0.5185	11.86/0.3713	9.77/0.5185	11.29/0.3193	
ADAIR Cui et al. (2024)	12.92/0.5456	14.46/0.4783	10.93/0.5576	12.72/0.4079	
DFPIR Tian et al. (2025a)	13.32/0.5643	15.68/0.4815	15.63/0.6599	14.74/0.3871	
<b>DAIR (Ours)</b>	<b>17.63/0.7080</b>	<b>17.94/0.6486</b>	<b>17.13/0.7180</b>	<b>14.77/0.5898</b>	
<i>Improvement</i>	<b>+2.64/+0.0737</b>	<b>+1.59/+0.0658</b>	<b>+1.06/+0.0059</b>	<b>+0.87/+0.0469</b>	

### B.1.2 DENOISING

Our experiment assesses the generalization of image denoising models under variable noise conditions, addressing limitations of prior works that train on fixed noise levels, leading to overfitting. We retrained baseline methods and our DAIIR model using random Gaussian noise on DIV2K Agustsson & Timofte (2017) and evaluated on unseen datasets, BSD100 Martin et al. (2001) and Urban100 Kim et al. (2016). Table 8 illustrate performance comparison across these datasets and noise levels ( $\sigma = 15, 25, 50$ ). Notably, baseline models showed inconsistent performance; Restormer struggled at higher noise, DiffUIR Zheng et al. (2024) excelled on BSD100 at  $\sigma=50$  but failed elsewhere, on six-task common AIR settings. Notably, MP-based methods, such as PromptIR Vaishnav et al. (2023), underperformed in the absence of precise noise-level prompts. This inconsistent performance, particularly among MP-based methods, underscores their inability to effectively segregate degradations, even on homogeneous tasks. In contrast, DAIIR consistently achieved higher scores, with improvements of up to +2.2 dB PSNR at high noise levels, highlighting its superior robustness and ability to effectively understand degradations, thereby validating the effectiveness of its latent prior encoding.

Table 8: Performance comparison across datasets and noise levels. Best results in **bold red**, second best underlined.

Method	DIV2K			BSD100			Urban100		
	$\sigma=15$ PSNR↑/SSIM↑	$\sigma=25$ PSNR↑/SSIM↑	$\sigma=50$ PSNR↑/SSIM↑	$\sigma=15$ PSNR↑/SSIM↑	$\sigma=25$ PSNR↑/SSIM↑	$\sigma=50$ PSNR↑/SSIM↑	$\sigma=15$ PSNR↑/SSIM↑	$\sigma=25$ PSNR↑/SSIM↑	$\sigma=50$ PSNR↑/SSIM↑
Uformer Wang et al. (2022)	31.71/0.9265	29.16/0.8753	25.46/0.7351	33.28/0.9219	30.61/0.8635	33.28/0.9219	31.52/0.9387	29.13/0.8944	25.15/0.7664
Restormer Zamir et al. (2022)	<u>27.38/0.8567</u>	23.44/0.6825	16.62/0.3646	28.32/0.8385	23.73/0.6373	31.59/0.8937	28.11/0.8873	23.67/0.7304	16.52/0.4315
AIRNet Li et al. (2022)	<b>32.91/0.9377</b>	<b>30.52/0.9095</b>	<b>27.07/0.8307</b>	<b>34.20/0.9333</b>	<b>31.83/0.8986</b>	<b>27.03/0.7000</b>	<b>33.19/0.9506</b>	<b>31.00/0.9324</b>	<b>27.46/0.8665</b>
PromptIR Vaishnav et al. (2023)	28.84/0.8464	25.90/0.7300	21.45/0.5164	30.04/0.8295	27.03/0.7007	30.61/0.8634	29.23/0.8755	26.05/0.7734	21.23/0.5685
DiffUIR Zheng et al. (2024)	19.92/0.8065	15.95/0.6774	14.34/0.5435	21.78/0.7909	17.41/0.6917	31.99/0.9122	18.28/0.7967	14.86/0.6701	13.67/0.5496
ADAIR Cui et al. (2024)	32.51/0.9412	30.10/0.9075	26.80/0.8174	34.06/0.9354	31.59/0.8937	14.07/0.4531	32.74/0.9514	30.33/0.9233	26.72/0.8420
DFPIR Tian et al. (2025a)	22.13/0.8095	21.57/0.7585	20.43/0.6234	21.77/0.8164	21.47/0.7535	21.48/0.7533	22.36/0.8182	21.80/0.7759	21.48/0.7533
<b>DAIR (Ours)</b>	<b>33.08/0.9541</b>	<b>30.62/0.9252</b>	<b>27.25/0.8555</b>	<b>34.48/0.9468</b>	<b>31.99/0.9122</b>	<b>31.83/0.8988</b>	<b>33.23/0.9623</b>	<b>30.82/0.9395</b>	<b>27.30/0.8796</b>
<i>Improvement</i>	<b>+0.17/+0.0164</b>	<b>+0.10/+0.0157</b>	<b>+0.18/+0.0248</b>	<b>+0.28/+0.0135</b>	<b>+0.16/+0.0136</b>	<b>-0.16/-0.0134</b>	<b>+0.04/+0.0117</b>	<b>-0.18/+0.0071</b>	<b>-0.16/+0.0131</b>

### B.2 MORE VISUAL RESULTS

Fig. 7 presents visual results for denoising, deraining, and dehazing tasks, comparing our method with ADAIR Cui et al. (2024), DFPIR Tian et al. (2025a), degraded inputs, and reference images. These examples demonstrate that our approach consistently achieves clearer and more accurate restorations, closely matching the reference images and outperforming baselines across all degradation types.

Fig. 8 presents more visual results for compound degradations (e.g., low-light + haze + rain, haze + rain), comparing our method with ADAIR Cui et al. (2024), DFPIR Tian et al. (2025a), degraded

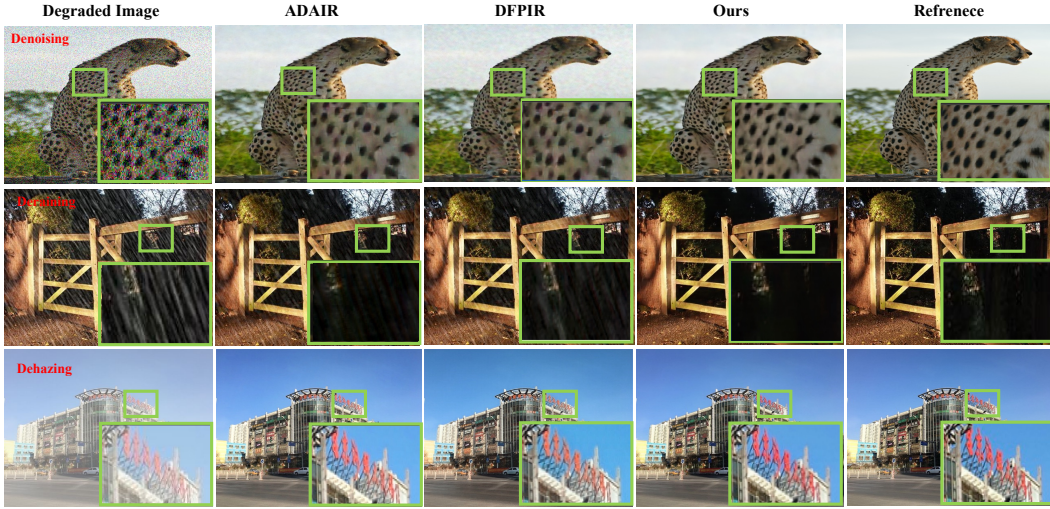


Figure 7: Visual comparisons of common image restoration, including denoising, deraining, and dehazing. Our method consistently delivers clearer and more accurate outputs, closely matching the reference images and outperforming ADAIR and DFPIR.

inputs, and reference images. Our approach consistently delivers clearer and more accurate restorations, outperforming baselines in challenging compound degradation settings.

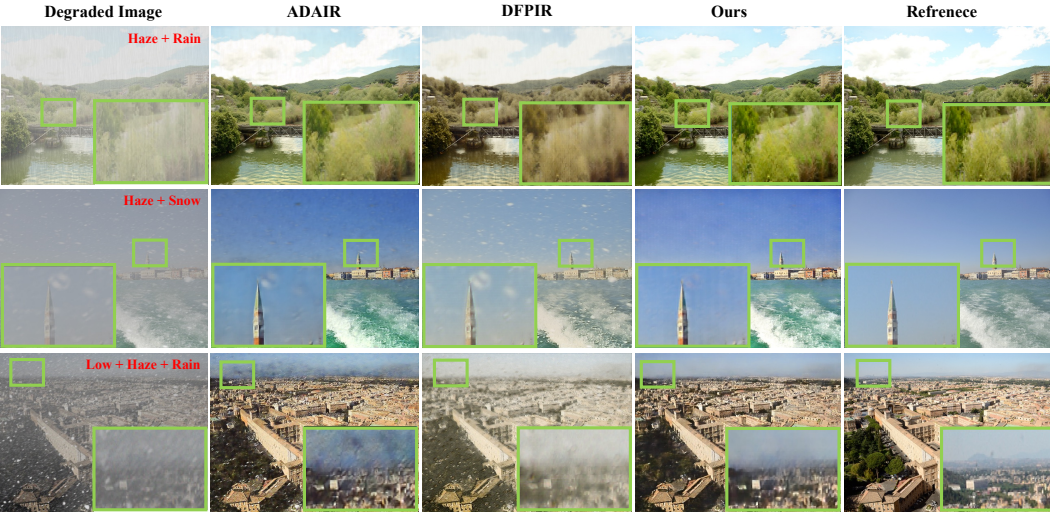


Figure 8: Visual comparisons of compound image restoration results for challenging scenarios, including haze + rain, haze + snow, and low-light + haze + rain. Our method consistently delivers clearer and more accurate outputs, closely matching the reference images and outperforming ADAIR and DFPIR.

### B.3 INFERENCE BENCHMARKING

Table 9 presents the inference speed of image restoration models, evaluated on lower-mid hardware (RTX 3060) using full-precision weights (FP32). Our DAIR model consistently achieves the fastest processing times, highest FPS, and superior throughput across various image sizes, outperforming all baseline AIR models. Notably, DAIR matches or surpasses the single-task model like Uformer (**43.86G**) Wang et al. (2022), which is significantly lighter compared to the existing AIR methods. These results highlight DAIR’s efficiency, demonstrating its ability to deliver SOTA restoration

Table 9: Inference speed comparison across different image restoration models. Best results in **bold red**, second best underlined.

Model	128×128			256×256			512×512		
	Time (ms)↓	FPS↑	Throughput (MP/s)↑	Time (ms)↓	FPS↑	Throughput (MP/s)↑	Time (ms)↓	FPS↑	Throughput (MP/s)↑
Uformer Wang et al. (2022)	31.07	<u>32.19</u>	0.53	<u>58.08</u>	<u>17.22</u>	1.13	<u>203.83</u>	<b>4.91</b>	<b>1.29</b>
PromptIR Vaishnav et al. (2023)	65.62	15.24	0.25	180.31	5.55	0.36	707.17	1.41	0.37
ADAIR Cui et al. (2024)	71.01	14.08	0.23	191.50	5.22	0.34	732.94	1.36	0.36
DFPIR (with CLIP) Tian et al. (2025a)	70.08	14.27	0.23	184.33	5.43	0.36	714.20	1.40	0.37
DFPIR (dummy text) Tian et al. (2025a)	67.88	14.73	0.24	184.12	5.43	0.36	714.38	1.40	0.37
<b>DAIR (Ours)</b>	<b>20.55</b>	<b>48.67</b>	<b>0.80</b>	<b>55.20</b>	<b>18.12</b>	<b>1.19</b>	220.92	4.53	1.19

quality while maintaining faster speed and practicality for real-world applications, even on modest hardware setups.

#### B.4 DOWNSTREAM VISION TASKS (OBJECT DETECTION)

A primary objective of AIR is enhancing downstream vision task performance Cui et al. (2024); Jiang et al. (2025), yet existing AIR methods lack benchmarking on such tasks due to insufficient annotated datasets. To address this critical gap, we created a comprehensive evaluation framework by annotating 3,000 test images across six common degradations (lowlight Sharif et al. (2025), de-raining Fu et al. (2017), dehazing Li et al. (2018), desnowing Li et al. (2020), denoising Agustsson & Timofte (2017), and deblurring Nah et al. (2017)). Our annotation process leveraged the paired nature of these datasets by first annotating ground truth reference images and transferring these annotations to their corresponding corrupted counterparts, ensuring consistency and reliability. We then enhanced these degraded images using several baseline AIR restoration methods and systematically evaluated their performance using the YOLOv12-Large Tian et al. (2025b) object detection model. This novel benchmarking approach provides the first quantitative assessment of how different restoration techniques impact object detection performance, offering valuable insights for developing AIR methods optimized for real-world computer vision applications.

Table 10: Performance comparison of object detection models. Best results in **bold red**, second best underlined.

Method	Average Precision (AP)			AP by Object Size		
	IoU=0.50:0.95	IoU=0.50	IoU=0.75	Small	Medium	Large
Uformer Wang et al. (2022)	28.0	30.2	29.4	36.5	26.9	27.3
Restformer Zamir et al. (2022)	<u>31.7</u>	<u>34.1</u>	<u>33.2</u>	37.5	<u>28.7</u>	<u>32.4</u>
AIRNet Li et al. (2022)	30.2	32.7	31.8	35.8	26.4	30.3
PromptIR Vaishnav et al. (2023)	30.9	33.3	31.9	<u>41.8</u>	28.6	30.6
ADAIR Cui et al. (2024)	28.9	31.2	30.2	38.4	28.8	28.1
DFPIR Tian et al. (2025a)	27.9	30.0	29.3	26.6	25.5	29.8
<b>DAIR (Our)</b>	<b>34.9</b>	<b>37.3</b>	<b>36.4</b>	<b>44.9</b>	<b>30.8</b>	<b>35.1</b>
<i>Improvement</i>	<i>+3.2</i>	<i>+3.2</i>	<i>+3.2</i>	<i>+3.1</i>	<i>+2.0</i>	<i>+2.7</i>

Table 10 presents a comprehensive performance comparison of various image restoration methods for object detection tasks. Our proposed DAIR method demonstrates superior performance across all evaluation metrics, achieving the highest Average Precision (AP) scores of **34.9%** at IoU=0.50:0.95, **37.3%** at IoU=0.50, and **36.4%** at IoU=0.75, surpassing the second-best method (Restformer Zamir et al. (2022)) by a significant margin of **3.2 percentage points**. DAIR also excels in detecting objects of varying sizes, achieving notably high AP scores on small (**44.9%**), outperforming PromptIR's **41.8%**, medium (**30.8%**), and large (**35.1%**) objects. The consistent improvements across all metrics highlight DAIR's effectiveness in enhancing image quality for downstream object detection, with an **average improvement of 3.2 percentage points** over SOTA methods. These results demonstrate DAIR's robust capability to address diverse degradation scenarios while preserving essential visual information for accurate object detection.

## C UNSEEN TASK GENERALIZATION

A key motivation behind the proposed latent-prior DAIIR framework is its ability to generalize to diverse, previously unseen degradations. To validate this capability, we extensively evaluate DAIIR under cross-domain and out-of-distribution scenarios, including underwater image enhancement Peng & Cosman (2019), medical image perceptual enhancement Uhlen et al. (2010), medical image denoising Rezvantalab et al. (2018), real-world denoising Abdelhamed et al. (2018), and unseen real-world low-light enhancement Sharif et al. (2025). Notably, all evaluations are performed using a DAIIR model trained only on common degradations, without any TS fine-tuning or external guidance. In addition to the visual results, we summarized the quantitative score with no-reference metrics: NIQE Mittal et al. (2013), MUSIQ Ke et al. (2021), and LPIPS Zhang et al. (2018b).

### C.1 REAL-WORLD DENOISING

Table. 8 and Figure 9 illustrate the performance of the proposed method on real-world noisy images Abdelhamed et al. (2018). In well-exposed scenes, DAIIR performs only denoising, preserving natural brightness and contrast. However, when inputs exhibit low-light characteristics (as commonly observed in SSID-like datasets Abdelhamed et al. (2018)) along with noise, the latent descriptor guides DAIIR to jointly suppress noise and enhance brightness. Thus, DAIIR adaptively performs denoising and enhancement without prompts or handcrafted rules.

Table 11: Image Quality Metrics for Real-world Noise Dataset. Best results in **bold red**.

Method	Image Quality Metrics		
	NIQE ↓	MUSIQ ↑	LPIPS ↓
Input	5.57	61.31	0.81
<b>Enhanced (Our)</b>	<b>4.24</b>	<b>69.37</b>	<b>0.80</b>
Improvement	+1.33	+8.06	+0.01

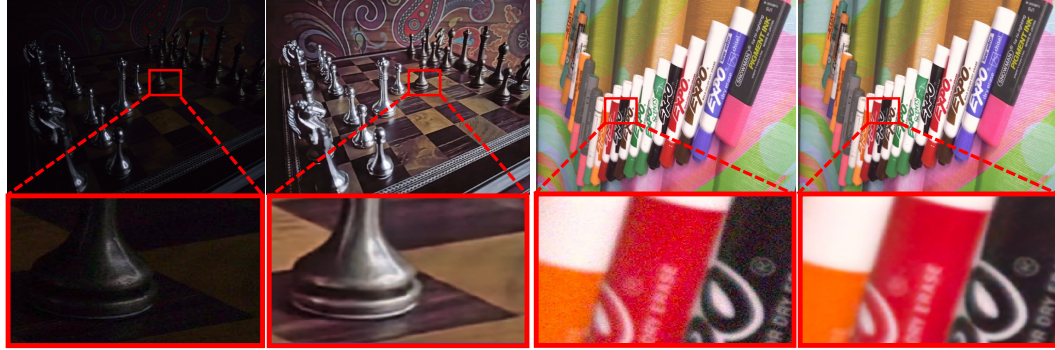


Figure 9: Real-world denoising results. Left: low-light noisy scenes where DAIIR jointly performs denoising and LLIE automatically, without user input. Right: well-lit, noisy scenes where DAIIR performs only denoising.

### C.2 UNDERWATER IMAGE ENHANCEMENT

We further evaluate DAIIR on underwater images, a domain unseen during training. As shown in Figure 10, the model adapts to varying underwater degradations, including haze-like scattering (left examples) and low exposure (right examples). Despite never being trained on underwater data, DAIIR enhances visibility and color fidelity, demonstrating strong cross-domain generalization driven by its latent prior representation. Table 12 further details DAIIR’s performance on underwater image enhancement.



Figure 10: Underwater image enhancement. DAIr generalizes to haze-like and low-exposed underwater degradations, improving contrast and color balance without domain-specific training.

Table 12: Image Quality Metrics for Underwater Image Enhancement. Best results in **bold red**.

Method	Image Quality Metrics		
	NIQE ↓	MUSIQ ↑	LPIPS ↓
Input	3.83	53.35	<b>0.70</b>
<b>Enhanced (Our)</b>	<b>3.78</b>	<b>54.05</b>	0.70
<i>Improvement</i>	+0.05	+0.70	+0.00

### C.3 UNSEEN LOW-LIGHT IMAGE ENHANCEMENT

We evaluate DAIr on real-world low-light images captured with unknown hardware and distributions (e.g., LSD-U Sharif et al. (2025)) unseen during training. Figure 11 and Table 13 demonstrate that the latent prior effectively encodes degradation properties, enabling robust out-of-distribution LLIE.



Figure 11: Unseen real-world low-light enhancement. DAIr can enhance illumination and structure in previously unseen low-light scenes without artifacts or over-enhancing the scenes.

Table 13: Image Quality Metrics for Real-world Lowlight Enhancement. Best results in **bold red**.

Method	Image Quality Metrics		
	NIQE ↓	MUSIQ ↑	LPIPS ↓
Input	4.47	62.33	0.81
<b>Enhanced (Our)</b>	<b>4.14</b>	<b>62.51</b>	<b>0.81</b>
<i>Improvement</i>	+0.33	+0.18	+0.00

### C.4 MEDICAL IMAGE PERCEPTUAL ENHANCEMENT

We also study cross-domain perceptual enhancement on microscopic medical images Uhlen et al. (2010), which often suffer from poor contrast and weak structural saliency Sharif et al. (2022). Despite having no exposure to this modality during training, DAIr enhances perceptual quality by improving local contrast and clarity while preserving natural textures (Figure 12). These results demonstrate that the latent prior generalizes to structurally distinct domains. Table 14 presents the corresponding quantitative improvements.

### C.5 MEDICAL IMAGE DENOISING

Finally, we evaluate DAIr on medical image denoising using a dataset not seen during training, specifically dermatoscopic imagery Rezvantalab et al. (2018). As shown in Figure 13, DAIr ef-



Figure 12: Perceptual enhancement of microscopic medical images. DAIR improves contrast and structural visibility in unseen medical imagery without TS training.

Table 14: Image Quality Metrics for Perceptual Enhancement. Best results in **bold red**.

Method	Image Quality Metrics		
	NIQE ↓	MUSIQ ↑	LPIPS ↓
Input	13.94	37.06	<b>0.63</b>
<b>Enhanced (Our)</b>	<b>9.68</b>	<b>41.50</b>	0.79
<i>Improvement</i>	<b>-4.26</b>	<b>+4.44</b>	<b>-0.16</b>

fectively suppresses noise while preserving diagnostically relevant textures and edges, without requiring manual prompting. Table 15 illustrates the performance of DAIR on unseen medical image denoising.

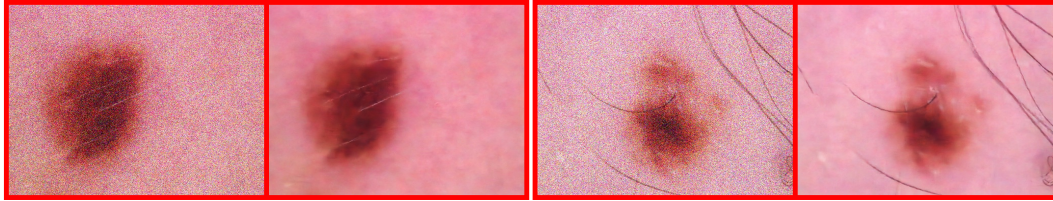


Figure 13: Medical image denoising. DAIR reduces noise and preserves fine structural details in previously unseen medical data, operating without guidance or fine-tuning.

Table 15: Image Quality Metrics for Medical Noise Reduction. Best results in **bold red**.

Method	Image Quality Metrics		
	NIQE ↓	MUSIQ ↑	LPIPS ↓
Input	16.99	21.93	0.82
<b>Enhanced (Our)</b>	<b>12.64</b>	<b>25.17</b>	<b>0.70</b>
<i>Improvement</i>	<b>+4.35</b>	<b>+3.24</b>	<b>+0.12</b>

## D LIMITATION AND FUTURE SCOPE

Despite the significant improvement of our proposed DAIR method over existing approaches on both common and compound degradations, as well as its performance on unseen tasks, we observed certain limitations. Figure 14 illustrates some failure cases of our method on unseen tasks. Specifically, in extreme low-light conditions (under 5 lux), artifacts were observed in homogeneous spatial regions, such as cloud-free skies. Additionally, in underwater image enhancement, the method occasionally produced over-enhanced results in tricky scenes. These observations highlight areas that require further investigation, which we plan to address in future studies.

Moreover, the proposed method was tested on lower-mid desktop environments. In contrast, AIR demonstrates significant potential for deployment on edge hardware. As part of future work, we plan to optimize DAIR for edge hardware by employing techniques such as low-bit quantization and mixed-precision inference. Furthermore, integrating vision tasks with AIR for practical applications presents another exciting direction for future research on DAIR.



Figure 14: Example of failure cases. Left: visual artifacts on the spatial region in extreme low-light conditions, right: over-enhancement of the underwater image.